CdZnTeSe: A promising material for radiation detector applications

Utpal N. Roy and Ralph B. James
Savannah River National Laboratory, Aiken, SC 29808, USA

Abstract:

The quest for cost-effective, high performing radiation detector materials operable at ambient temperature has continued for more than three decades. One key to lower the overall detector cost of production is a high degree of compositional homogeneity. Spatial homogeneity of the charge-transport properties of the detector material is also essential for increasing the yield and active volume of high-performance detectors. Despite its commercial success as a room-temperature radiation detection material, CdZnTe (or CZT) suffers from a lack of compositional homogeneity on both a micro- and macro-scale and the presence of spatial inhomogeneity in the material's charge-transport properties. The underlying reasons for the spatial inhomogeneity in the charge-transport properties of CZT are the presence of high concentrations of sub-grain boundary (dislocation walls) networks and secondary phases (Te-rich inclusions) on a micro-scale and the segregation of zinc during growth on a macro-scale. This book chapter focuses on the presence of performance-limiting defects in CZT that hinder the yield and cost of high-quality detectors and have restricted wide-spread deployment for a variety of potential applications, particularly for uses of large-volume detectors where the demands on material perfection are significantly greater. In the recent past, the addition of selenium in CZT matrix was found to be very effective in a drastic reduction of Te-rich secondary phases and dislocation networks, while demonstrating little or no Se segregation during ingot growth. This chapter will provide an overview of recent developments on the quaternary CdZnTeSe material as a potential next-generation detector material operable at room temperature.

Introduction:

The availability of radiation detection technology with energy dispersive spectroscopic capability in the energy range of X- and gamma-rays operating at room temperature has opened a wide variety of applications in homeland security, nonproliferation, medical imaging, astrophysics and high energy physics[1-9]. The enormous potential uses have motivated researchers to develop better materials and processing technology to meet the growing demands worldwide. The properties of candidate materials for radiation detector applications are very stringent and multi-pronged. The basic requirement for the ideal radiation detector material is a high average effective atomic number, hence a high electron density for increased stopping power of the high energy radiation. In addition, the constituent elements should be non-radioactive to ensure low noise. For room-temperature operation the foremost criterion is sufficiently high band gap energy to achieve an electrical resistivity on the order of $>10^{10}$ ohm-cm. Such high resistivity is required to decrease the dark current in order to enhance the signal-to-noise ratio. Furthermore, as the radiation detector users demand devices with larger thickness to enhance detection efficiency of high energy gamma rays, the material should have adequately high mobility-lifetime product ($\mu\tau$) to ensure complete charge collection. The operating thickness of the functional detector can be increased with increased $\mu\tau$ value assuming the internal electric field can be maintained. From the standpoint of the crystal growth, the material should be able to grow from congruent melt at a relatively low temperature and be capable of scale-up to allow for growth of large volume ingots to keep a lower cost of production. The grown material should be compositionally homogeneous, possess very less defects (intrinsic and extrinsic) and more importantly possess spatial uniformity of the charge transport characteristics. The chemical and physical stability of the metal-to-semiconductor junction is also an important aspect for prolonged lifetime of the detector. Over the last three decades, only a handful of semiconductor materials have been discovered with the desired attributes, and CdTe, CdZnTe (CZT), HgI_2 and TlBr are the most prominent ones[10-14]. In the recent years, perovskites are evolving as a promising material for room-temperature semiconductor detector (RTSD) applications for high energy radiation[15]. John et al.[16] listed a comprehensive list of possible radiation detector materials in a review article. Each of these materials however do suffer from unique issues associated with difficulty of crystal growth, high concentrations of defects and device stability.

Despite intense research for the ideal material globally for more than three decades, CZT still remains the gold standard and dominates the commercial sector. It is to be noted that CZT is a byproduct of many years of R&D on CdTe. CdTe has multiple uses and has long been known as a substrate material for IR and night vision applications, and since the 1970s it has been regarded as a potential material for nuclear radiation detector applications[17 (and references therein)]. In later years Zn was added to the CdTe matrix for better lattice matching to HgCdTe for night vision applications, while Zn was added to CdTe to increase the band-gap of the material to achieve higher resistivity and prevent polarization effects associated with Cl-doped CdTe radiation detectors. Most of the CZT material used today for radiation detector applications contains ~10 atomic % of Zn in the CdTe matrix. CZT based radiation detector applications gained serious momentum from early 1990's after the onset of commercialization. The initial commercial process started with high pressure Bridgman grown detector grade CZT material[18,19]. Around the same time in 1990, Triboulet et al.[20] demonstrated the growth of CdTe and ZnTe by Cold Traveling Heater Method (CTHM), and in 1994 the same group successfully grew CZT by the CTHM technique. In the later years CTHM became commonly known as the Traveling Heater Method

(THM). The THM technique uses the growth of the material from a Te-rich solution, which allows the ingots to grow well below its melting point. The THM technique offers several advantages as compared to melt grown techniques. Because of the lower temperature growth, the ingots possess less defects and thermal stress. The investigators also confirmed that THM-grown ingots show better axial and radial compositional homogeneity with a higher purity as compared to melt-grown ingots[21]. Based on the THM growth technique, Redlen Technologies was founded in 1999 for commercial production of detector-grade CZT. As a consequence of the advantages and successes on the newly invented technique, other companies began using THM to produce detector-grade CZT materials. Over time the THM technique has proven to be the most viable technique to grow CdTe and CZT commercially, and very large diameter ingots up to 10 cm can be produced[22]. Despite the intense research for the last three decades, CZT still possesses several shortcomings that severely limit the widespread deployment, especially for large-volume detectors. Although these shortcomings have been very difficult to fully resolve, the quality of CZT material has improved considerably since its early years, and the production cost has steadily decreased. The presence of high concentrations of sub-grain boundary networks and Te inclusions remains as a long-standing issue associated with CZT material. These defects act as the charge trapping and recombination centers and severely affect the uniformity of the charge transport characteristics of the material resulting in limitations on the thickness of high-performing detectors. Incremental increases in performance have been demonstrated as the size and concentration of Te inclusions has decreased through modifications in the growth and post-processing conditions. In addition to these extended structural defects, CZT suffers heavily from axial and radial compositional inhomogeneity due to the non-unity segregation of Zn in the CdTe matrix[23]. The compositional non-uniformity affects the overall yield of detector-grade material from the grown ingot. In addition the compositional gradient is known to impose considerable strain in the CZT ingot[6,24]. The present article will discuss the sub-grain boundary networks in CZT and their effect on device performance. One effective way to mitigate such defects is by adding selenium into the CZT matrix, which can increase the yield of high-quality detector grade material from a grown ingot by reducing the large-scale variations in the alloy composition.

Sub-grain boundaries and their networks in CZT:

Unlike conventional elemental semiconductors such as Si and Ge, various structural defects are present in CZT, which adversely affect the charge transport characteristics of the material and the performance of fabricated devices. Sub-grain boundaries and their networks and Te inclusions are the most prominent extended defects in CZT, and they are the main defects responsible for compromising the detector performance and lowering the yield of high-quality detector grade material from a given ingot. The broadening of photo-peaks in detectors is often attributed to the presence of sub-grain boundaries and their networks and Te inclusions, although point defects and leakage current can be problematic as well. Sub-grain boundaries are in principle dislocation walls, where the dislocations are arranged along the boundary walls[25,26]. In most cases, these sub-grain boundaries and dislocation walls are arranged in cellular structures because of polygonalization[27] and are highly decorated in CZT material. The configuration of dislocation walls is typically called the sub-grain boundary network. These dislocations are visible after preferential etching of polished surfaces. The sub-grain boundary networks can also be observed by X-ray topographic images, preferably in reflection mode. Figure 1a shows a preferentially etched CZT sample surface with dimensions of 9x3 mm^2 and the corresponding X-ray topographic image (Fig. 1b). The dark lines in the cellular structure are arrangements of dislocations along the sub-grain boundary in the

CZT sample. The density of sub-grain boundaries is particularly high for this sample. The dark spots in the ellipses denoted in Fig. 1a are commonly known as punching defects, which form on sites of Te inclusions that have been removed by post-growth annealing process. The X-ray topographic image of the same sample also shows the presence of sub-grain boundaries and their network with the appearance of dark and bright lines. The punching defects appear as white spots on the X-ray topographic images as highlighted inside the ellipses. As depicted in Fig 1, the sub-grain boundary networks are often found to be randomly distributed in the CZT matrix, and the sub-grain boundaries are also known to be decorated with Te inclusions[25, 28]. The sub-grain boundaries are invisible through infrared (IR) transmission microscopy. Since Te inclusions are opaque in the infrared wavelength range, sub-grain boundaries and their networks often can be tracked through the decoration of Te inclusions seen in IR transmission images[25,28]. The sub-grain boundary network was also observed by bright field Transmission Electron Microscopy (TEM) by Zeng et al.[28]; they also confirmed the decoration of sub-grain boundaries by Te precipitates as shown in Fig. 2. The sub-grain boundaries and their networks are possibly the most concerning

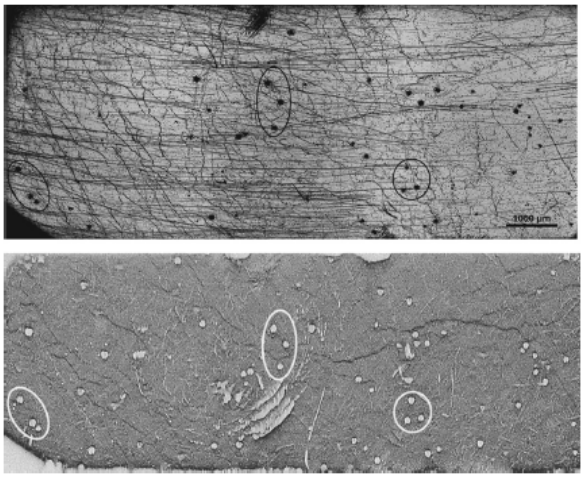

Fig. 1. Sub-grain boundaries and prismatic dislocations, usually generated around Te inclusions after post-growth annealing, are apparent on the surface of a 9x3 mm^2 area of the crystal treated with the Nakagawa-etching technique (top) and with X-ray diffraction topography (bottom). The circles denote the prismatic dislocations defects seen in both images. (Taken from A. Bolotnikov et al., Reference # 25).

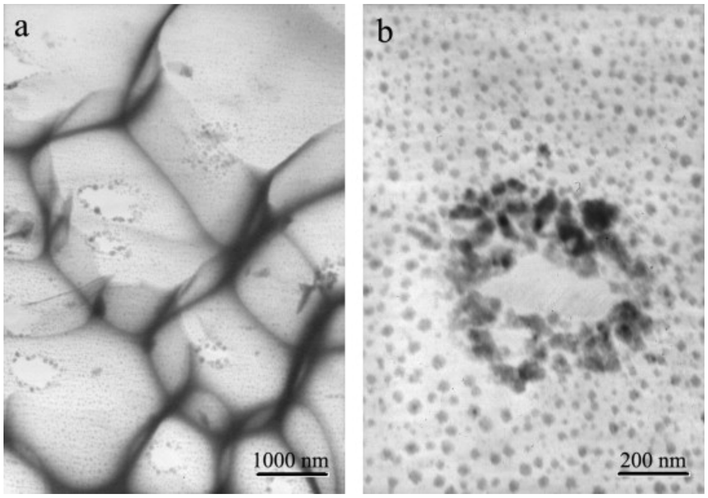

Figure 2. Sub-grain boundary networks and their Te precipitates a) Bright field image of sub-grain boundary networks, and b) Agglomerated Te precipitates present along sub-grain boundary networks. (Taken from D. Zeng et al., Reference # 28).

defects in CZT material among those affecting the detector performance. The sub-grain boundaries and their networks were found to be present in CZT samples irrespective of growth techniques. Bolotnikov et al.[25] reported the presence of sub-grain boundaries and their networks in CZT samples by X-ray topographic measurements produced from seven different vendors across the globe. The dislocations and their networks are known to introduce during growth/solidification and subsequent cooling process due to thermal stress related to the inherent poor thermo-physical properties of CdTe/CZT. Moreover, the energy of creation of dislocations and stacking faults are inversely proportional to the ionicity[6]. This makes the highly ionic II-VI crystal lattice very sensitive to any strain and prone to introduction of stress-related defects. Thus, the drastic improvement of CdTe/CZT material is limited due to its inherent poor thermo-physical properties. The sub-grain boundaries and their network cannot be removed by post-growth annealing; however, eliminating the Te inclusions from the CZT matrix by post-growth annealing is a common practice in CZT detector manufacturing process. Unfortunately, the process is known to produce large star-like defects (punching defects) at the locations of relatively large Te inclusions in post-annealed samples. The star-like defects are invisible in an IR transmission measurement, but they are detectable by charge collection mapping, preferential etching, and X-ray topographic experiments. Depending on their concentration and size, these star-like defects can severely hamper the charge-transport properties[29] and the device performance[30]. Furthermore, Te inclusions are known to be surrounded by a dense field of dislocations, and those remain even after removing the inclusions by thermal annealing[27]. Because of the high concentrations of defects at the dislocation walls viz. sub-grain boundaries are prone to accumulate impurities[25] in addition to the Te inclusions. In addition to the dislocations itself, all these impurities and the Te inclusions are responsible for creating charge trapping centers at different binding energies within the band-gap of the material. It has been observed that the dislocations introduced by deformation of CZT produces a trap state at an energy of ~0.27 eV[31]. Te inclusions are reported to introduce a trap level at 1.1 eV above the valence band[32]. Impurities are responsible for shallow and/or deep trap states depending on their position in the energy gap and the Fermi level. For example, the impurities from group III produce shallow levels and the transition elements are accountable for deep states. Most of these defects act as electron trapping centers and can severely hamper the charge-transport characteristics of the material depending on their concentration and electron capture cross section[26,27,33]. Carini et al.[33] demonstrated direct evidence of the charge loss due to the presence of Te inclusions. The mobility-lifetime product for electrons [$(\mu\tau)_e$] in CZT can vary over a larger range of between $(0.2\text{-}20)\times10^{-3}$ cm^2/V for the regions with Te inclusions compared to the clear regions that are relatively free from large inclusions[33]. This indicates that the random distribution of these localized defects in CZT matrix imposes severe spatial charge-transport inhomogeneity, which eventually broadens the photo-peaks and degrades the detector performance.

The spatial variation of charge-transport characteristics was evaluated by high spatial resolution X-ray response mapping with a spatial resolution of better than 10 µm[33,34]. The experiments were conducted using collimated synchrotron light source of beam size ~10x10 µm^2. Planar CZT detectors were raster scanned across the whole area with a step size of a few microns, and the detector response was registered at each point of interaction for an incident low energy X-ray beam with an energy of 7-40 keV. The pulse height (i.e., the channel numbers at each point) was then mapped over the whole area of the sample. The schematic of the experimental set up is shown in Figure 3. The experimental setup and procedure are detailed elsewhere[33,34] as reported by Carini et al.[33] and Camarda et al[34]. Charge loss or incomplete charge collection due to the localized defects such as Te inclusions and sub-grain boundaries and their networks were also reported to be dependent on the applied bias, as was demonstrated by Camarda et al.[34] Figure 4a shows IR image of etched surface of a typical CZT sample revealing different defects such as dislocation walls, viz. sub-grain boundaries and star-shaped defects. The corresponding X-ray response map of the planar detector fabricated with the same sample of dimensions 12x5x5 mm^3 is shown in Fig. 4b under an applied bias of 500 V using a 30-keV energy synchrotron beam. Non-uniform charge

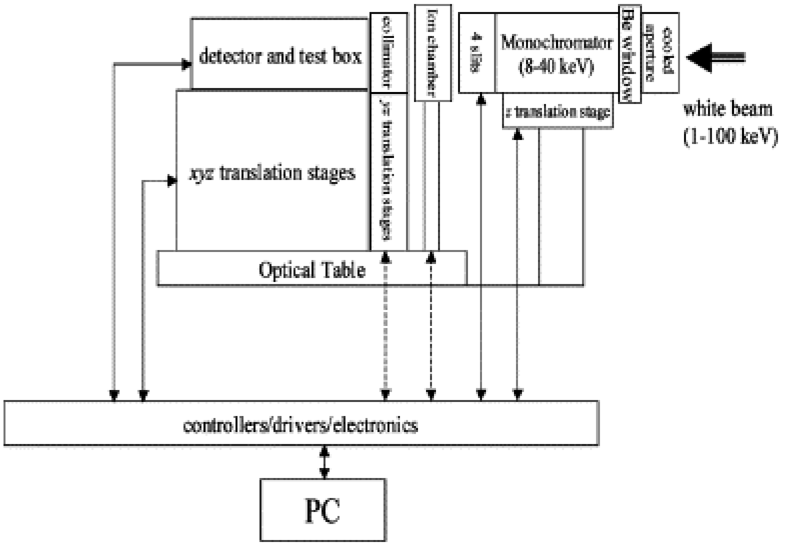

Figure 3. Block diagram of the X-ray response mapping system (Taken from G. A. Carini et al., Ref. #33).

collection was observed throughout the entire area. The bright area corresponds to higher charge collection efficiency, while the grey or dark areas are associated with reduced charge collection due to the presence of localized defects. The appearance of dark lines in Fig. 4b shows the presence of sub-grain boundaries (dislocation walls) as a result of incomplete charge collection at the boundary walls. Severe charge loss is also evident for the star-shaped defects as shown in Fig. 4b. Fairly good correlation between the regions of low charge collection and the locations of defects in the crystal displayed in Figs. 4a and 4b was observed[35].

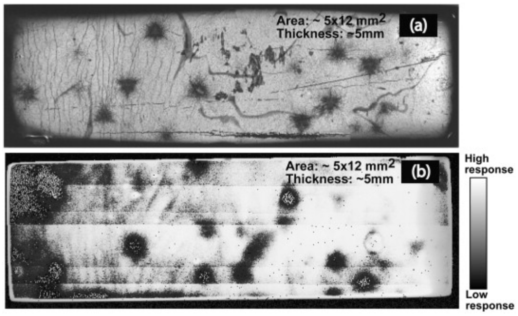

Figure 4. a) IR image of etched surface of a CZT sample and b) raster-scanned image of X-ray response map of the same CZT sample. Sample dimensions: 12x5x5 mm^3. (Taken from A. Hossain et al., Ref. 35).

Different pulse heights are produced at different locations of the detector sample due to the random distribution of extended defects, which smears the resulting photopeak of the detector after integrating detectors responses over the entire active volume. The performance degradation becomes more prominent with increased thickness. Thus, the spatial homogeneity of charge transport characteristics in detector material is critically important in achieving high-quality detectors and maximizing their yield. Apart from spatial charge-collection uniformity, high-quality detector material also demands spatial homogeneity of radiation-induced charge generation, and the presence of extended defects and other band-gap variations also adversely affects such uniformity. The effect of sub-grain boundaries on the performance of Frisch grid detectors was very prominent as compared for two different detector samples of the same dimensions[25]. Both the detectors showed the presence of a high density of sub-grain boundary networks, while the sample containing a greater number of major sub-grain boundaries displayed larger broadening of the photopeaks and low energy continuum[25]. The presence of sub-grain boundaries/dislocation walls in CdTe family entails a serious issue for medical imaging applications as well. Buis et al.[36] demonstrated that the image of a cowry shell taken with CdTe pixelated detector contained various lines corresponding to dislocation walls and sub-grain boundaries. The defects had to eliminate after the flat-field correction. It is thus necessary to develop material free from large Te inclusions and sub-grain boundary networks to avoid the need for charge-loss correction schemes, which impact measurement time, power consumption and cost effectiveness. Moreover, material free from the secondary phase and sub-grain boundary networks drastically enhances the yield of high-quality detectors with can potentially lead to a substantial cost reduction.

Effects of Se addition to the CdZnTe matrix:

Most II-VI compounds are prone to strain and extended defects in as-grown ingots due to their high ionicity. Due to the high ionicity of CdTe at 0.55[6], it is not surprising that CdTe ingots show the presence of sub-grain boundaries and their networks and residual strain. The ionicity is inversely proportional to the energy of creation for dislocations and for stacking faults[6]. Higher ionicity and the poor thermo-physical properties of CdTe limit the improvement of the material quality and makes it difficult to grow large-volume high quality crystals with less defects. In addition to the growth-related defects, CdTe also suffers from a lower band-gap, which hinders achieving high resistivity material on the order of $>10^{10}$ ohm-cm. The ternary material CZT came up as the consequence of the desire to improve the properties of CdTe. Adding Zn in CdTe matrix offered several advantages for different applications. For example, adding Zn in CdTe provides better lattice matching substrates to HgCdTe epilayers for IR or night vision applications. For detector applications, the band-gap is enhanced to help satisfy the required resistivity of over 10^{10} ohm-cm for making low-noise nuclear detectors with improved performance. The most beneficial reason for adding Zn in CdTe is the higher binding energy of the Zn-Te bond and lower ionicity. Thus, the addition of Zn in CdTe was reported to reduce the dislocation density and sub-grains and enhance the micro-hardness due to the lattice hardening effect of Zn.[6, 37-39] If we define CdTe as the first-generation radiation detector material, then the ternary compound CZT is the second-generation detector material. Although some lattice hardening was observed after addition of Zn in the CdTe matrix, CZT still comprises a relatively high density of sub-grain boundaries and their networks as discussed in the last section, which affects the yield of high-quality detectors and limits the wide spread deployment of CZT especially for large-volume detectors.

Despite incremental improvements over the last three decades, it has been extremely difficult to overcome the inherent poor thermo-physical properties of CdTe/CZT and grow large-volume crystals free from sub-grain boundaries and their networks. To improve the crystallinity and increase the volume of defect-free material, one approach has been to pursue isoelectronic doping as an effective means for solid-solution hardening. The substrate community observed a profound reduction of sub-grain boundaries and their networks after doping CdTe by as low as 0.4 % (atomic) selenium, and they also showed that solid solution hardening with Se is more effective than with Zn (see, for example, Refs. 7 and 40). Later, the advantage of Se doping was realized by adding it to the CZT matrix for substrate applications[41]. At the early stage of CZT development in 1994, Fiederle et al.[42] reported a better $\mu\tau$ product for electrons (4.2×10^{-4} cm^2/V) and superior charge-collection efficiency for Bridgman-grown $CdTe_{0.9}Se_{0.1}$ (CTS) crystals compared to CZT. In recent years the addition of selenium in the CdTe matrix was also shown to greatly reduce the sub-grain boundaries and produce crystals free from sub-grain boundary networks, plus a reduction in the concentration of Te-rich secondary phases and an improvement in the compositional uniformity[43-45].

White Beam X-ray Diffraction Topography (WBXDT), especially in the reflection mode is very sensitive in revealing the presence of sub-grain boundaries and their networks. The technique is also sensitive to localized strain present in the crystal. The localized strain results in lattice distortion, which consequently deforms the topographic image. In general, X-ray topographic images in the reflection mode reveal the presence of sub-grain boundaries as the appearance of white and dark lines based on the tilt angle of adjacent sub-grains. The white and dark lines appear due to the separated and overlapping diffracted images of adjacent sub-grains respectively, subject to angle of the adjacent sub-grains.

The experimental procedure for WBXDT is rather simple. An intense X-ray beam with an energy range of 6–40 keV from a synchrotron light source reaches the sample's surface, commonly at a grazing incident angle of 4–5 degrees. The diffracted images are recorded on high-resolution X-ray films. The schematic of the setup is shown in Figure 5.

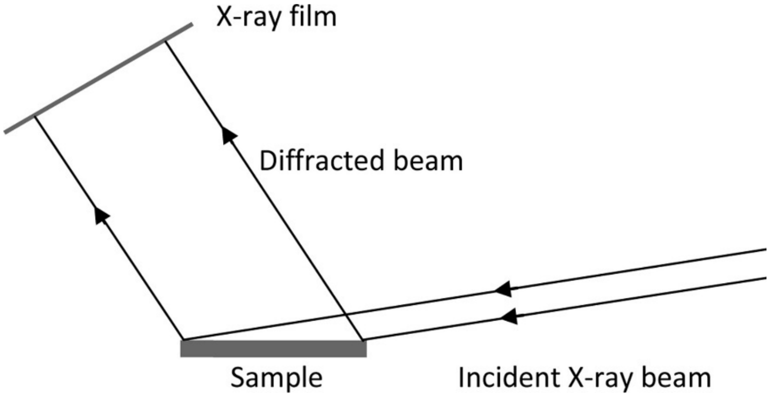

Fig. 5. Schematic of the X-ray diffraction topographic experimental setup in the reflection mode. (Taken from U. N. Roy et al., Ref. #45)

Significant improvements of the microstructural properties regarding sub-grain boundaries and their networks were demonstrated by adding selenium to the CdTe matrix[6,40]. They confirmed the resulting CdTeSe to be free from sub-grain boundary networks by using preferential etching to reveal dislocations. Recently, we also confirmed the efficacy of Se addition in CdTe matrix using X-ray topographic studies[45]. Figure 6a shows the results for a lapped wafer along the length of a THM-grown $CdTe_{0.9}Se_{0.1}$ ingot. The arrow indicates the growth direction. The left end is ~1.5 cm from the tip, and the right end is ~1.5 cm from the top of the ingot. The occurrence of a few twins in the material is evident from this figure. The wafer contains two large grains indicated as (a) and (b), as shown in Fig. 6a. The X-ray topographic investigation was carried out for these two large grains. The topographic experiments were carried out on a mirror-finished polished surface followed by etching in a bromine-methanol solution. X-ray topography, especially in the reflection mode, is very sensitive to the surface preparation. Care was taken to remove surface damage from the polishing process by etching the polished samples prior to the experiments. The X-ray diffraction topographic images of the grains "a" and "b" as indicated in Fig. 6a are shown in Figs. 6b and c, respectively. As shown in Fig. 6b, the ingot surface touching the ampoule wall shows little or no deformation in the topographic image indicating that the contact is relatively stress free. A slight deformation on the ingot surface touching the ampoule wall is evident from Fig. 6c depicting a small amount of stress-induced lattice deformation. Ampoule walls very commonly

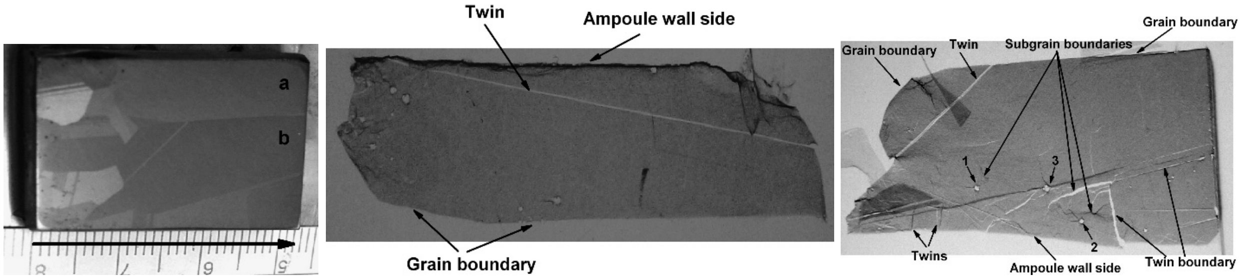

(a) **(b)** **(c)**

Fig. 6. a) The wafer cut along the length from the central part of the THM-grown $CdTe_{0.9}Se_{0.1}$ ingot. The arrow shows the growth direction. b) X-ray diffraction topographic image of the grain "a", and c) "b" of the CTS sample. (Taken from U. N. Roy et al., Ref. #45).

introduce strain in melt-grown ingots, especially in CdTe-based compounds[46]. Severe lattice distortions, as observed by the streaky nature of the X-ray topographic images near the periphery of the wafers, were also observed for contact-less vapor grown CdTe and CZT[47,48]. The distortion near the periphery for the contact-less wafer was however reported to be due to possible turbulence in the vapor flow around the periphery of the grown ingot[48]. Due to their inherent structure, twins are very straight in nature. Thus, twins are a good reference frame to observe the presence of any residual stress present in the crystal. Any stress present in the crystal results in localized lattice distortion, hence the twins in the topographic image would be deformed. As shown in Fig. 6b, the topographic image shows the presence of twinning almost diagonally across the entire grain, which is very straight. The appearance of the straight twins in the X-ray topographic image indicates that the entire grain is practically strain free. A similar straight appearance of straight twin lamellae is also evident on the left upper part of the grain "b" as shown in Fig. 6c. No sub-grain boundary was detected in the X-ray topographic image of the grain "b" as shown in Fig. 6b, while few sub-grain boundaries are evident near the lower middle part of the grain "b". These sub-grain boundaries are shown in Fig. 6c as the appearance of white and dark lines in the topographic image. However, no cellular structure viz. sub-grain boundary networks were observed in any part of the ingot, which agrees well with earlier results demonstrated back in the mid 1990s[6,29]. The addition of selenium in the CdTe matrix proved to be an effective solution-hardening element in producing ingots free from sub-grain boundary networks and with greatly reduced residual thermal stress.

Despite profound improvement of the higher quality, the material does not qualify for radiation detector applications, especially for uses demanding high detection efficiency where lower leakage currents are required. Although the band-gap of CdSe is higher than CdTe, the band gap of the ternary decreases with Se concentration up to a concentration of ~40%[49]. The bowing of the band gap with Se concentration was ascribed to a compositional disorder effect[49]. Thus, the band-gap of the ternary turns out to be lower than that for CdTe, which restricts the material from attaining the requisite electrical resistivity for room temperature operation. To achieve the advantages of selenium and also obtain a larger band-gap than CTS, we pursued a quaternary compound by adding selenium to $Cd_{0.9}Zn_{0.1}Te$. Different compositions were evaluated with varying selenium concentrations from 1.5% to 7% (atomic), while keeping the concentration of zinc constant at the value of 10% (atomic). For all the tested concentrations, the resulting CZTS ingots were found to be free from a sub-grain boundary network. Figure 8 shows an optical photograph of a grain (left) from a two-inch $Cd_{0.9}Zn_{0.1}Te_{0.93}Se_{0.07}$ wafer cut perpendicular to the growth axis for an ingot grown by the THM, and the corresponding X-ray topographic image of the same grain shown in the right side of the photograph[50]. In order to evaluate the effectiveness of selenium as a solution hardening agent, the ingot was naturally cooled to room temperature after the completion of growth to force introduction of thermal stress. It is to be noted that no lattice distortion was observed near the periphery of the wafer touching the ampoule wall, as indicated by the blue arrow, depicting the absence of any stress introduced from the ampoule wall. This observation agrees well with prior measurements for CTS ingots. However, slight lattice distortion was indeed observed at the wall contact of the CTS ingots, while in case of CZTS, we did not observe any lattice distortion in the X-ray topographic image of the wafer touching the ampoule wall. This observation suggests that the presence of Se and Zn is more effective in arresting the introduction of thermal stress than compared to individually doped Se or Zn in CdTe ingots. Furthermore, the undistorted twins in the X-ray topographic image, as indicated by the green arrows in Fig. 7, provide evidence that the material is free from any thermal stress. The undistorted grain boundaries of the X-ray topographic image also corroborate the effectiveness of selenium as an effective solid solution hardening element in CZT matrix. The material was observed to be free from sub-grain boundary networks with the presence of very few sub-grain boundaries as illustrated in Fig. 7, albeit the ingot was cooled at a faster rate.

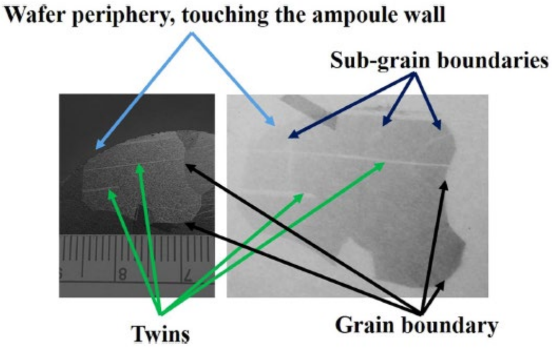

Figure 7. Optical photograph of the grain (left) and the corresponding X-ray topographic image of the grain. (Taken from U.N. Roy et al., Ref. # 50).

To counter the large thermal stress associated with the higher temperature growth process, similar studies were also carried out with melt-grown CZTS ingots with the same composition. Very large thermal stress is known to introduce during the growth and cooling processes of melt-grown ingots by the Bridgman method as compared to the THM. We recently reported an X-ray topographic study of vertical Bridgman grown $Cd_{0.9}Zn_{0.1}Te_{0.93}Se_{0.07}$ ingot with a diameter of 4 cm[51]. Figure 8 shows the photograph of lapped wafers cut perpendicular to the ~11-cm-long $Cd_{0.9}Zn_{0.1}Te_{0.93}Se_{0.07}$ ingot with diameter of 4 cm grown by the vertical Bridgman technique[51]. As is evident from Fig. 8, the ingot is composed of two mono-crystals with one very large grain except for the conical part of the ingot. A few twins are visible near the conical part of the ingot, and most of the ingot is twin-free. As mentioned earlier, all the X-ray topographic diffraction experiments

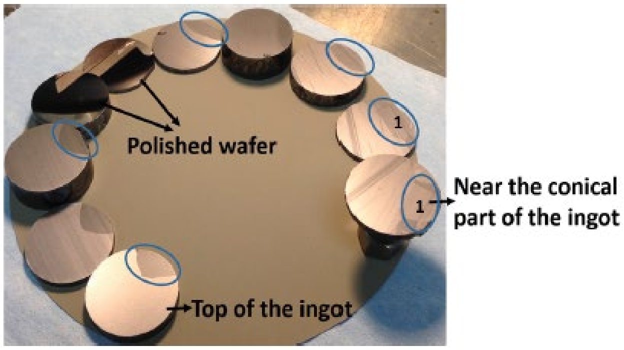

Fig. 8. Optical photograph of the wafers cut perpendicular to the ingot axis. (Taken from U.N. Roy et al., Ref. # 51).

were carried out on mirror-finished surfaces followed by bromine-methanol etching. X-ray topographic analyses were carried out for three different wafers taken from top, middle and bottom (~ 1.5 cm above the conical part) parts of the ingot. The very top of the Bridgman grown ingot undergoes the maximum thermal stress since this part of the ingot remained at the highest temperature for the longest amount of time during growth as well as during the subsequent cooling process.

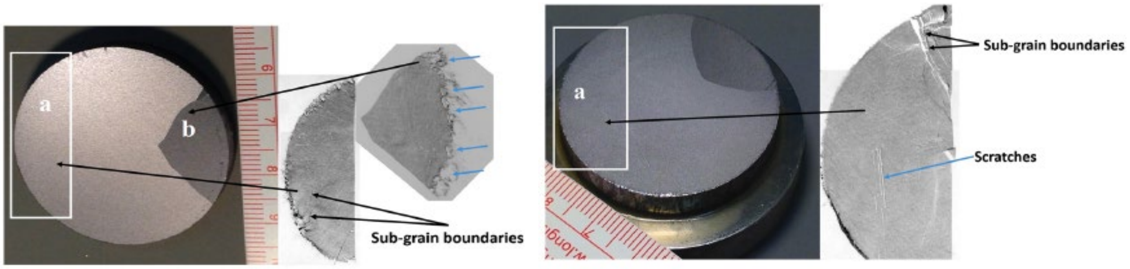

(a) **(b)**

Figure 9. a) Photograph of the 4-cm diameter $Cd_{0.9}Zn_{0.1}Te_{0.93}Se_{0.07}$ lapped wafer cut from the very top of the ingot, and the X-ray topographic images of the region denoted by the white rectangle and the grain on the right side of the wafer. b) Photograph of the bottom part of the wafer and the corresponding X-ray topographic image of the region denoted by the white rectangle (The white rectangles and the corresponding X-ray topographic images are not to scale). Thickness of the wafer: 6.3 mm. (Taken from U.N. Roy et al., Ref. # 51).

The ingot was cooled to room temperature at the rate of $\sim 4^0$C/hr after the completion of the growth process. Figure 9 shows the wafer cut from the top of the ingot and the associated X-ray topographic images. Fig. 9a shows the top surface of the ingot. The top of the ingot was barely lapped to a flat surface in order to investigate the X-ray topographic characteristics of the top-most part of the ingot. The X-ray topographic image of the region “a” denoted by the white rectangle in Fig. 9a shows slight lattice distortion near the periphery of the wafer (i.e., the region touching the ampoule wall). The streaky nature of the X-ray topographic image (for grain “b”) for the region contacting the ampoule wall illustrates the presence of high lattice distortion. Note that the shape of the grain “b” in the topographic image is undistorted depicting the absence of overall thermal stress in the wafer. Figure 9b shows the opposite face of the top wafer of thickness ~6.3 mm; the X-ray topographic image of the portion indicated as a rectangle “a” is also shown. One outstanding feature of the X-ray topographic image is the absence of any lattice distortion on the periphery of the wafer. Even for the portion near the top of the ingot, very few sub-grain boundaries were evident from the topographic image, and no sub-grain boundary network was seen. As expected, the X-ray topographic analyses for the wafers from the middle and the lower parts of the ingot also showed the absence of significant lattice distortion, hence lower thermal stress along the periphery of the wafers for those regions in touch with the ampoule wall. The optical photograph and their corresponding X-ray topographic images are shown in Figs. 10 and 11, respectively. The overall undistorted topographic image also exemplifies the absence of thermal stress in the crystal. Very

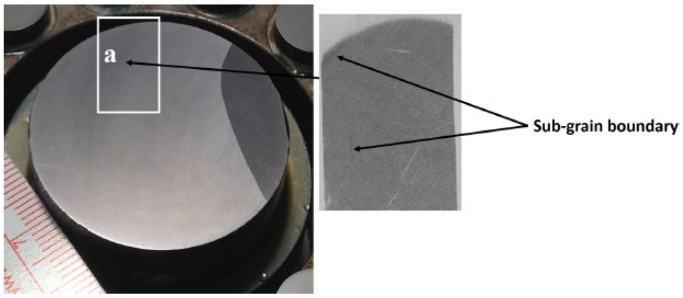

Figure 10. Photograph of the 4-cm diameter $Cd_{0.9}Zn_{0.1}Te_{0.93}Se_{0.07}$ lapped wafer cut near the middle of the ingot and the X-ray topographic image of the region denoted by the white rectangle. (The white rectangle and the corresponding X-ray topographic images are not to scale). (Taken from U.N. Roy et al., Ref. # 51).

few sub-grain boundaries were observed for all the wafers from different parts of the ingot. The straight nature of the twin in the topographic image shown in Fig. 11 also indicates that the wafer is stress free. The defect indicated inside the blue ellipse in the topographic image (Fig. 11) is possibly a sub-grain boundary in a closed loop.

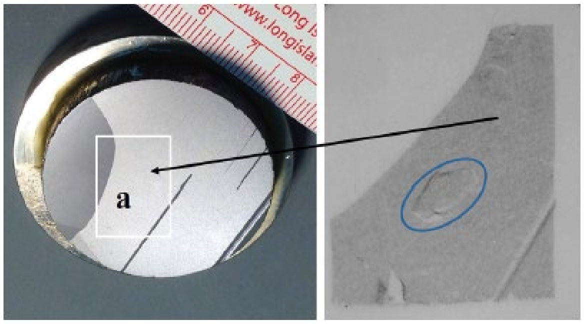

Figure 11. Photograph of the 4-cm diameter Cd$_{0.9}$Zn$_{0.1}$Te$_{0.93}$Se$_{0.07}$ lapped wafer cut from bottom of the ingot and the X-ray topographic image of the region denoted by the white rectangle. (The white rectangle and the corresponding X-ray topographic images are not to scale). (Taken from U.N. Roy et al., Ref. # 51).

The circular nature of the periphery of the wafers, the undeformed grain boundaries and straight nature of the twins in the topographic images implies the absence of overall thermal stress in the wafers as well as the ingots. The features were found to be similar for both THM and Bridgman grown CZTS ingots. The addition of selenium in the CZT matrix thus proved to be an effective solution-hardening element in arresting the formation of sub-grain boundaries and their networks. It is thus evident that addition of selenium in CdZnTe successfully resolves persistent unsolved issues associated with difficulties encountered in the CZT crystal growth and provides significant material improvements of importance for radiation-detection applications.

In conclusion selenium was found to play a significant role in improving the material quality of CZT. The microhardness of the new quaternary compound CZTS was observed to be significantly higher[52] as compared to CdTe and CZT. The compositional homogeneity was also greatly enhanced in CTS and CZTS as compared to CZT[43,50,53]. The concentrations of the secondary phases viz. Te-inclusions were also observed to be greatly reduced after adding selenium to the CdTe and the CZT matrix[44,50,53,54]. The reduced performance-limiting defects and enhanced compositional homogeneity ensure higher spatial charge transport homogeneity in CZTS material resulting in increased yield of high-quality detectors. The achieved energy resolution of Frisch-grid detectors fabricated from as-grown CZTS ingots at 662 keV was in the range of 1±0.1%[52,53]. CZTS is thus found to be a very promising material with tremendous potential to replace CZT due a better yield of high-quality detector material and a reduced cost of production. Due to the multi-faceted advantages, CZTS has attracted quick attention from the commercial sector for medical imaging applications. Very recently Yakimov et al.[55] reported superior detector quality as compared to conventional CZT for the intensity of high flux X-rays expected in many medical imaging applications. Thus, considering the overall superior material properties and homogeneity of CZTS, the material shows potential to supersede CZT in the future, particularly as the purity of the Se is further increased.

References:

1. T. E. Schlesinger et al., "*Cadmium zinc telluride and its use as a nuclear radiation detector material*", Materials Science and Engineering R 32, 103 (2001).

2. G. Yang and R. B. James, "*Applications of CdTe, CdZnTe, and CdMnTe Radiation Detectors"*, Physics, Defects, Hetero- and Nano-structures, Crystal Growth, Surfaces and Applications Part II, (EDAX. Triboulet R. *et al.*) 214 (Elsevier, 2009).

3. F. A. Harrison et al., "*The Nuclear Spectroscopic Telescope Array (NuSTAR) High-energy X-Ray Mission*", The Astrophysical Journal 770, 103 (2013).

4. H. S. Krawczynski et al., “ *X-ray polarimetry with the Polarization Spectroscopic Telescope Array (PolSTAR)*”, Astroparticle Physics 75, 8 (2016).

5. P. J. Slomka et al., “*Solid-State Detector SPECT Myocardial Perfusion Imaging*”, Journal of Nuclear Medicine 60, 1194 (2019).

6. R. Triboulet, “*Fundamentals of the CdTe and CdZnTe bulk growth*”, Phys. Status. Solidi (c) 5, 1556 (2005).

7. P. Rudolph, “*Fundamental studies on Bridgman growth of CdTe*”, Prog. Crystal Growth and Charact. 29, 275 (1994).

8. W. Jing and L. Chi, “*Recent advances in cardiac SPECT instrumentation and imaging methods*”, Physics in Medicine and Biology 64, 06TR01 (2019).

9. T. Sakamoto et al., “*The Second Swift Burst Alert Telescope Gamma-Ray Burst Catalog*”, The Astrophysical Journal Supplement Series 195, 1 (2011).

10. T. Takahashi et al., “*High-resolution CdTe detector and applications to imaging devices*”, IEEE Trans. on Nucl. Sc. 48, 287 (2001).

11. J. MacKenzie et al., “*Advancements in THM-Grown CdZnTe for Use as Substrates for HgCdTe*”, J. Elect. Materials 42, 3129 (2013).

12. K. Iniewski, “*CZT detector technology for medical imaging*”, J. of Instrumentation 9, 1 (2014).

13. A. Kargar et al., “*Charge collection efficiency characterization of a* HgI_2 *Frisch collar spectrometer with collimated high energy gamma rays*”, Nucl. Instrum. Methods Phys. Res. A 652, 186 (2011).

14. K. Hitomi et al., “*TlBr Capacitive Frisch Grid Detectors*”, IEEE Trans. on Nucl. Sc. 60, 1156 (2013).

15. Y. He, et al., “*High spectral resolution of gamma-rays at room temperature by perovskite $CsPbBr_3$ single crystals*”, Nature Communications 9, 1609 (2018).

16. P. M. Johns and J. C. Nino, “*Room temperature semiconductor detectors for nuclear security*”, J. Appl. Phys. 126, 040902 (2019).

17. T. Takahashi and S. Watanabe, “*Recent progress in CdTe and CdZnTe detectors*”, IEEE Trans. on Nucl. Sc. 48, 950 (2001).

18. C. Szeles and E. E. Eissler, “*Current issues of high-pressure Bridgman growth of semi-insulating CdZnTe*”, MRS Symp. Proc., Vol. 484, 309 (1998).

19. C. Szeles et al., “*Development of the High-Pressure Electro-Dynamic Gradient Crystal-Growth Technology for Semi-Insulating CdZnTe Growth for Radiation Detector Applications*”, J. Elect. Materials 33, 742 (2004).

20. R. Triboulet et al., *““Cold travelling heater method”, a novel technique of synthesis, purification and growth of CdTe and ZnTe”*, J. Crystal Growth 101, 216 (1990).

21. A. El Morki et al., “*Growth of large, high purity, low cost, uniform CdZnTe crystals by the “cold travelling heater method”*”, J. Crystal Growth 138, 168 (1994).

22. H. Shiraki et al, “*THM Growth and Characterization of 100 mm Diameter CdTe Single Crystals*”, IEEE Trans. on Nucl. Sc. 56, 1717 (2009).

23. N. Zhang et al., “*Anomalous segregation during electrodynamic gradient freeze growth of cadmium zinc telluride*”, J. Crystal Growth 325, 10 (2011).

24. C. Perfeniuk et al., “*Measured critical resolved shear stress and calculated temperature and stress fields during growth of CdZnTe*”, J. Crystal Growth 119, 261 (1992).

25. A.E. Bolotnikov et al., “*Characterization and evaluation of extended defects in CZT crystals for gamma-ray detectors*”, J. Cryst. Growth 379, 46 (2013).

26. A.E. Bolotnikov et al., "*Extended Defects in CdZnTe Radiation Detectors*", IEEE Trans. on Nucl. Sc. 56, 1775 (2009).

27. C. Szeles et al., "*Advances in the crystal growth of semi-insulating CdZnTe for radiation detector applications*", IEEE Trans. on Nucl. Sc. 49, 2535 (2002).

28. D. Zeng et al., "*Transmission electron microscopy observations of twin boundaries and sub-boundary networks in bulk CdZnTe crystals*", J. Cryst. Growth 311, 4414 (2009).

29. G. Yang et al., "*Post-growth thermal annealing study of CdZnTe for developing room-temperature X-ray and gamma-ray detectors*", J. Cryst. Growth 379, 16 (2013).

30. A. E. Bolotnikov et al., "*CdZnTe position-sensitive drift detectors with thicknesses up to 5 cm*", Appl. Phys. Lett. 108, 093504 (2016).

31. N. Krsmanovic et al., "*Electrical compensation in CdTe and CdZnTe by intrinsic defects*", SPIE Proceedings 4141, 219 (2000).

32. R. Gul et al., "*A comparison of point defects in* $Cd_{1-x}Zn_xTe_{1-y}Se_y$ *crystals grown by Bridgman and traveling heater methods*", J. Appl. Phys. 121, 125705 (2017).

33. G. A. Carini et al., "*High-resolution X-ray mapping of CdZnTe detectors*", Nucl. Instrum. Methods A 579, 120 (2007).

34. G. S. Camarda et al., "*Polarization Studies of CdZnTe Detectors Using Synchrotron X-Ray Radiation*", IEEE Trans. on Nucl. Sc. 55, 3725 (2008).

35. A. Hossain et al., "*Extended defects in CdZnTe crystals: Effects on device performance*", J. Cryst. Growth 312, 1795 (2010).

36. C. Buis et al., "*Effects of Dislocation Walls on Image Quality When Using Cadmium Telluride X-Ray Detectors*", IEEE Trans. on Nucl. Sc. 60, 199 (2013).

37. R. Triboulet, Crystal Growth Technology, "*CdTe and CdZnTe Growth*", Ed. H. J. Scheel and T. Fukuda, Wiley, 373 (2003).

38. K. Guergouri et al., "*Solution hardening and dislocation density reduction in CdTe crystals by Zn addition*", J. Cryst. Growth 86, 61 (1988).

39. D. Imhoff et al., "*Zn influence on the plasticity of* $Cd_{0.96}Zn_{0.04}Te$", J. Phys. France 1, 1841 (1991).

40. C. J. Johnson, "*Recent Progress In Lattice Matched Substrates For HgCdTe Epitaxy*", SPIE 1106, 56 (1989).

41. A. Tanaka et al., "Zinc and selenium co-doped CdTe substrates lattice matched to HgCdTe", J. Crystal Growth 94, 166 (1989).

42. M. Fiederle et al., "*Comparison of CdTe,* $Cd_{0.9}Zn_{0.1}Te$ *and* $CdTe_{0.9}Se_{0.1}$ *Crystals: Application for γ- and X-ray detectors*", J. Crystal Growth 138, 529 (1994).

43. U. N. Roy et al., "*Growth of* $CdTe_xSe_{1-x}$ *from a Te-rich solution for applications in radiation detection*", J. Crystal Growth 386, 43 (2014).

44. U. N. Roy et al., "*High compositional homogeneity of* $CdTe_xSe_{1-x}$ *crystals grown by the Bridgman method*", Appl. Phys. Lett. Materials 3, 026102 (2015).

45. U. N. Roy et al., "*Evaluation of* $CdTe_xSe_{1-x}$ *crystals grown from a Te-rich solution*", J. Cryst. Growth 389, 99 (2014).

46. Ching-Hua Su et al., "*Crystal growth and characterization of CdTe grown by vertical gradient freeze*", Mat. Sci. Eng. B 147, 35 (2008).

47. W. Palosz et al., "*The effect of the wall contact and post-growth cool-down on defects in CdTe crystals grown by 'contactless' physical vapour transport*", J. Cryst. Growth 254, 316 (2003).

48. C. K. Egan et al., "*Characterization of vapour grown CdZnTe crystals using synchrotron X-ray topography*", J. Cryst. Growth 343, 1 (2012).

49. L. Hannachi, and N. Bouarissa, "*Electronic structure and optical properties of* $CdSe_xTe_{1-x}$ *mixed crystals*", Superlattices and Microstructures 44, 794 (2008).

50. U. N. Roy et al., "*Role of selenium addition to CdZnTe matrix for room-temperature radiation detector applications*", Scientific Reports 9, 1620 (2019).

51. U. N. Roy et al., "*X-ray topographic study of Bridgman-grown CdZnTeSe*", J. Cryst. Growth 546, 125753 (2020).

52. J. Franc et al., "*Microhardness study of* $Cd_{1-x}Zn_xTe_{1-y}Se_y$ *crystals for X-ray and gamma ray detectors*", Materials Today Comm. 24, 101014 (2020).

53. U. N. Roy et al., "*Evaluation of CdZnTeSe as a high-quality gamma-ray spectroscopic material with better compositional homogeneity and reduced defects*", Sci. Rep. 9, 7303 (2019).

54. U. N. Roy et al., "*High-resolution virtual Frisch grid gamma-ray detectors based on as-grown CdZnTeSe with reduced defects*", Appl. Phys. Lett. 114, 232107 (2019).

55. A. Yakimov et al., "*Growth and characterization of detector-grade CdZnTeSe by horizontal Bridgman technique*", SPIE Proc. 11114, 111141N (2019).